JGR Earth Surface

RESEARCH ARTICLE
10.1029/2025JF008380

Observation and Prediction of Sand Ripple Geometry on a Sloped Bed Under Varying Combined Wave-Current Flows

Seok-Bong Lee[1,2], Meagan E. Wengrove[1], Matthieu A. de Schipper[3], Maarten G. Kleinhans[4], Gerben Ruessink[4], and Julia Hopkins[5]

[1]School of Civil and Construction Engineering, Oregon State University, Corvallis, OR, USA, [2]Now at School of Ocean Science and Engineering, John C. Stennis Space Center, The University of Southern Mississippi, Hattiesburg, MS, USA, [3]Faculty of Civil Engineering and Geosciences, Department of Hydraulic Engineering, Delft University of Technology, Delft, The Netherlands, [4]Department of Physical Geography, Faculty of Geosciences, Utrecht University, Utrecht, The Netherlands, [5]Department of Civil and Environmental Engineering, Northeastern University, Boston, MA, USA

Abstract We investigated quasi-2D sand ripple geometry (i.e., ripple height, ripple wavelength, and ripple asymmetry) on a mound subject to the influence of waves, currents, and combined wave-current flows. The results of this study quantify how ripple geometry is influenced by bed slope and combined wave-current flows. The geometry of the ripples is shown to depend on the combined wave-current flow ratio and the local bed slope. Under wave-only conditions, the wave-driven ripple length and height decreased as a function of depth and local slope. Under combined wave-current conditions, the ripples increased in height and wavelength on the stoss slope of the mound, and decreased on the lee slope of the mound. Existing ripple geometry predictors, developed for combined flows on flat sand beds, were unable to predict ripple geometry on the sloped bed accurately. We propose correction factors for ripple geometry predictors to account for slope effects and combined wave-current flow conditions. Applying the correction factors significantly improves the predictor performance for predicting ripple height, wavelength, and asymmetry on sloping beds.

Plain Language Summary We studied how sand ripples form and change on a sloped mound under the influence of waves, currents, and their combined effects. Our results show that ripple size and shape depend on both the flow conditions and the slope of the seabed. When only waves were present, ripples became smaller as water got deeper and the slope increased. When waves and currents worked together, ripples grew larger on the front side of the mound but became smaller on the back side. Existing models, which were designed for flat sandy areas, could not accurately predict ripple size on sloped beds. To fix this, we developed correction factors that improve the accuracy of these models, making them more reliable for predicting ripple patterns on sloping seabeds.

Key Points:

- The geometry of sand ripples (length, height, asymmetry) is shaped by the underlying slope and the relative influence of waves and currents
- Improving sand ripple geometry prediction on sloped beds involves adding local bed slope angle and wave to wave-current flow velocity ratio

Supporting Information:

Supporting Information may be found in the online version of this article.

Correspondence to:

S.-B. Lee,
leeseokb@oregonstate.edu

Citation:

Lee, S.-B., Wengrove, M. E., de Schipper, M. A., Kleinhans, M. G., Ruessink, G., & Hopkins, J. (2025). Observation and prediction of sand ripple geometry on a sloped bed under varying combined wave-current flows. *Journal of Geophysical Research: Earth Surface*, *130*, e2025JF008380. https://doi.org/10.1029/2025JF008380

Received 19 FEB 2025
Accepted 28 JUL 2025

Author Contributions:

Conceptualization: Seok-Bong Lee
Data curation: Seok-Bong Lee, Meagan E. Wengrove, Matthieu A. de Schipper, Julia Hopkins
Formal analysis: Seok-Bong Lee, Meagan E. Wengrove
Funding acquisition: Meagan E. Wengrove, Matthieu A. de Schipper
Investigation: Seok-Bong Lee, Meagan E. Wengrove, Matthieu A. de Schipper, Julia Hopkins
Methodology: Seok-Bong Lee, Meagan E. Wengrove
Project administration: Matthieu A. de Schipper
Resources: Meagan E. Wengrove, Matthieu A. de Schipper
Software: Seok-Bong Lee
Supervision: Meagan E. Wengrove, Matthieu A. de Schipper
Validation: Meagan E. Wengrove
Visualization: Seok-Bong Lee
Writing – original draft: Seok-Bong Lee

1. Introduction

Small-scale sand ripples are persistent bedform features in the nearshore zone. Their geometry (i.e., height, wavelength, asymmetry) influences bed roughness, which affects wave energy dissipation, near-bed boundary layer structure, turbulence intensity and sediment suspension (Brakenhoff, Schrijvershof, et al., 2020; Fredsoe & Deigaard, 1992; Nielsen, 1981, 1992; Soulsby, 2005; Styles & Glenn, 2000; Van Rijn, 1993; Wiberg & Harris, 1994). The nearshore environment is subject to combined wave-current flow conditions; as such the combined flow-driven small-scale ripple is common (Cataño-Lopera & García, 2006; Perillo et al., 2014). Field and laboratory experimental studies have been carried out to investigate sand ripple formation and geometry under combined wave-currents on a flat bed (Clifton & Dingler, 1984; Khelifa & Ouellet, 2000; Lacy et al., 2007; Li & Amos, 1998; Masselink et al., 2007; O'Donoghue et al., 2006; Ruessink et al., 2015; Soulsby et al., 2012; Tanaka & Dang, 1996; Traykovski, 2007; Wengrove et al., 2018, 2019; Wiberg & Harris, 1994). Based on these studies, analytical and empirical predictors have been suggested for subaqueous ripple geometry as a function of non-dimensional local hydrodynamic parameters (e.g., non-dimensionalized orbital diameter, median grain diameter, ripple steepness, etc.) for combined wave-current conditions (Khelifa & Ouellet, 2000; Li & Amos, 1998; Soulsby et al., 2012; Tanaka & Dang, 1996; Wengrove et al., 2018).

Ripple geometry is also shown to be influenced by the local bed slope (Damgaard et al., 2003; Lee et al., 2023; Wang & Yuan, 2018). On a sloped bed, a non-zero gravitational force alters the local bedload sediment flux and the incipient motion threshold of sediment (Baar et al., 2018; Damgaard et al., 1997). Observations of ripple

Writing – review & editing: Meagan E. Wengrove, Matthieu A. de Schipper, Maarten G. Kleinhans, Gerben Ruessink

geometric change on a sloped bed (from −20° to 20° slope angle) show that the height and wavelength of ripples increase in the presence of upslope currents and decrease in the presence of downslope currents (Damgaard et al., 2003). However, Damgaard et al. (2003) does not quantify ripple geometry change as a function of slope. Small-scale ripples superimposed on large-scale sloping morphologic features have been observed in flume experiments (Lee et al., 2023; Smith et al., 2017; Stansby et al., 2009) and in the field (Jones & Traykovski, 2019; Wengrove et al., 2022), but these studies do not report observations of ripple geometry as a function of slope angle. Until now, the influence of bed slope on ripple geometry has only been quantified in wave-driven (Lee et al., 2023; Wang & Yuan, 2018) and current-driven flows (Damgaard et al., 2003) separately, but not under combined wave-current conditions. Additionally, all ripple geometry predictors for ripples subject to combined wave-current flows neglect the influence of slope. We know that combined wave current flows and bed slope can influence ripple geometry (flow roughness) independently. As such, it is reasonable to assume that there may be a non-linear influence of combined wave-current flows and bed slope on ripple roughness characteristics. Additionally, we know that coastal hydrodynamic and morphodynamic models are sensitive to parameterized roughness for accurate estimates of sea surface elevation and phase, circulation intensity and direction, and sediment transport statistics (Hsu & Hanes, 2004; Lesser et al., 2004; Soulsby, 1997; Zijlema & Stelling, 2005). We also know that the coastal ocean composed of dynamic and sloping bathymetry and nearly always influenced by some combination of waves and currents (Dean & Dalrymple, 2004; Komar, 1977; Wright & Short, 1984). Therefore, our aim is to: (a) quantify the influence of slope on ripple geometry in combined wave-current driven flows and (b) provide a parameterization for estimating ripple geometry (wavelength, height, asymmetry) in combined wave-current flows on a sloped bed.

The manuscript is organized by first presenting the experimental methods (Section 2) and observations (Section 3) from a laboratory experiment where we observed ripple geometric development on a sloping sand mound under varying combined wave-current flows. Next, we choose and present existing ripple predictors formulated for combined wave-current flows on a flat bathymetry (Section 4.1) and report the performance (Section 4.3). We then propose a correction for the best performing ripple geometry predictor using the bed slope angle and wave to combined wave-current flow velocity ratio for better estimation of ripple height and wavelength (Section 4.4). We also propose a modification to the slope-induced asymmetry estimation for ripples in combined flows based on bed slope (Section 4.5). Finally, in the discussion (Section 5) we synthesize and expand upon our observations of the influence of bed slope and the wave-current velocity ratio on ripple geometry with a detailed schematic and context for this study with respect to scaling and morphodynamic modeling. The symbols and variables used throughout the study are summarized in Table 1.

2. Methods

2.1. Experimental Description

Data were collected during the MODEX experiment conducted in the Total Environment Simulator (TES) at the University of Hull in the UK. The TES flume is 12 m long, 6 m wide, and had a 0.4 m water depth. The flume can generate both waves and currents with a piston-type multi-directional wave-maker and a current pump, respectively. However, both monochromatic waves and unidirectional currents were generated in the same direction for this study. A perforated wave damping pad with artificial grass was deployed at the beach side of the flume to attenuate the waves and minimize wave reflection (Figure 1). A Gaussian-shaped sand mound, 1.5 m in diameter and 0.2 m in height, was deployed with well sorted sand of 0.215 mm median grain diameter (d_{50}) at the center of the flume. A Gaussian-shaped mound was used because it allowed us to evaluate the influence of various flow conditions on the same bathymetry, builds from past work of De Vriend (1987), is relatively simple to set up in morphologic change models, and for the case of this manuscript allows us to monitor the influence of a larger scale morphologic feature on small scale sediment transport processes. For the study presented herein, we focused on a quasi-2D slice through the center of the sand mound in the direction of the waves and currents, and therefore neglected the three-dimensionality of the mound. For the interested reader, figures of 3D morphologic change of the mound can be found in the Supplementary Information for this manuscript (See Text S2 and Figure S1 in Supporting Information S1).

A total of nine experiments were conducted during MODEX, involving unidirectional monochromatic waves, currents, and combined wave-current conditions of varying magnitudes (for more detailed experimental descriptions, see de Schipper et al. (2019)). Here we selected five experiments, including one wave-only, one current-

Table 1
Nomenclature Used in This Study

Symbol	Description
A	Semi-orbital excursion, $A = \frac{d_0}{2}$ (m)
a/b	Ripple asymmetry index (ratio of stoss to lee slope lengths)
$(a/b)_{corr}$	Corrected asymmetry index including wave-current effects
$(a/b)_{slp}$	Slope-induced asymmetry index
a_1, b_1	Fitted coefficients for height correction
a_2, b_2	Fitted coefficients for wavelength correction
D_*	Dimensionless grain size
d_0	Orbital excursion, $d_0 = \frac{u_w T}{\pi}$ (m)
d_{50}	Median sediment grain size (m)
Fr	Froude number, $Fr = \frac{V}{\sqrt{gh}}$
h	Water depth (m)
K	Slope transition smoothing function
p	Correction exponent ($p = u_w/u_{wc}$)
R_u, R_a	Orbital velocity skewness and asymmetry
S_f	Slope correction factor for bedload transport
T	Wave period (s)
U	Depth-averaged current velocity (m/s)
$u(t)$	Instantaneous velocity measured by ADV (m/s)
u_w	Near-bed wave orbital velocity amplitude (m/s)
u_{wc}	Combined wave-current velocity magnitude (m/s)
V_s	Volume of a single sediment grain (m^3)
α_c	Angle of repose (assumed 31°)
β	Local bed slope angle (degrees)
η	Ripple height (m)
η_{corr}, λ_{corr}	Corrected ripple height and wavelength (m)
η_{model}, λ_{model}	Original uncorrected ripple height and wavelength (m)
λ	Ripple wavelength (m)
ϕ_w, ϕ_c	Wave and current propagation directions (degrees)
ρ	Water density (kg/m^3)
θ_w	Wave-induced Shields parameter
θ_c	Current-induced Shields parameter
θ_{wc}	Combined wave-current Shields parameter
θ_{cr}	Critical Shields parameter

only, and three combined wave-current experiments (w>c, w∼c, w<c), to investigate the effect of a variable wave to combined wave-current flow velocity ratio on characteristic ripple geometry on a sloping bed (see Table 2). Each experiment consisted of 8–9 runs, and each run lasted 5–6 min for a total run time of 40–55 min for each experiment (see Table 2). To more explicitly describe the experimental process, let us consider the current-only flow experiment: An experiment consisted of first collecting the pre-lidar scan of the newly shaped mound in the empty basin. The basin was then filled with water. The first run and measurements were started by generating a current with velocity of 0.29 m/s. The current was stopped and intermediate measurements of morphologic change using sonar were collected (not shown). Then the same current condition was continued for 5 more min for the second run without re-setting the sand mound, and so on for a total of 8 runs (8 runs × 5 min per run = 40-min experiment). The basin was then drained and the post-lidar scan of the bathymetry was collected. Finally, the mound was re-set for the next experiment and the process re-started with hydrodynamic conditions set as defined in Table 2.

Instrumentation used for the analysis presented herein included three Nortek Acoustic Doppler Velocimeters (ADV) and a FARO Focus X330 lidar scanner. The ADVs collected three-dimensional water particle velocity at the overall morphologic change of the mound and ripples on the sandy bed. The full experiment deployed a larger array of ADVs and profiling ADVs, wave gauges, sonar, lidar, and cameras (for more details about full experiment instrumentation, see de Schipper et al. (2019) and Lee et al. (2019)).

2.2. Hydrodynamics

Flow conditions tested included a wave-only condition, three combined wave-current conditions, and a current-only condition (Figure 2, Table 2). The ADV measurements were time averaged to find the mean current velocity, $U = \overline{u(t)}$. With the mean current removed, the time-averaged wave orbital velocity magnitude (u_w) was estimated as the root-mean-square of the oscillatory velocity time-series:

$$u_w = \sqrt{2\overline{(u(t) - U)^2}}. \quad (1)$$

The ADV was positioned 10 cm above the mound top, and 25 cm above the flat bed. With the measurement locations available, we had to assume that the time-averaged current velocity from the ADV is similar to the depth-averaged current velocity at each measurement location along the mound length. However, to estimate the near-bed orbital wave velocity, we applied linear wave theory to attenuate the estimated u_w amplitude to the bed (Figure 3, see Text S1 in Supporting Information S1 for more details). Using U and u_w, the combined wave-current velocity was estimated as:

$$u_{wc} = \sqrt{u_w^2 + U^2 + 2u_w U|\cos(\phi_w - \phi_c)|} \quad (2)$$

where ϕ_w and ϕ_c represent the wave and current directions, respectively. Since the wave and current directions are the same in the experiment, this simplifies to $u_{wc} = u_w + U$. We then defined the wave to combined wave-current flow velocity ratio as u_w/u_{wc}.

The five experiments included in this manuscript were selected based on fairly similar combined wave-current Shields parameters, used to indicate a similar overall hydrodynamic energy imposed on the mound-top and

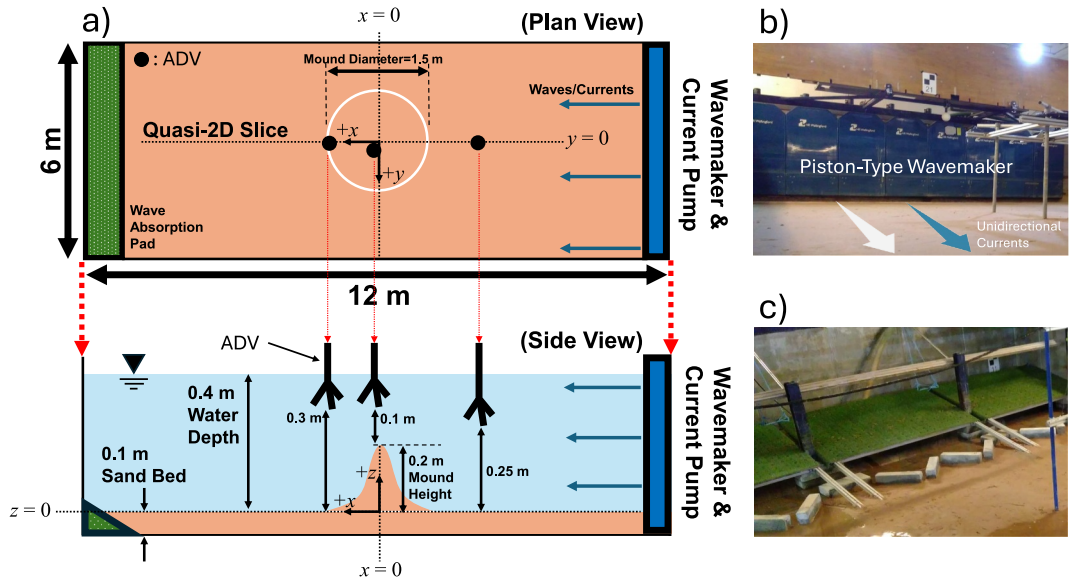

Figure 1. Schematic for experimental setup. (a) (top) Plan view of the flume with locations of the Acoustic Doppler Velocimeters (ADV) instruments. Longitudinal (x) and transverse (y) coordinates, and direction of the coordinates are shown. The center of the mound is set as $(x, y) = (0, 0)$. (bottom) Side view of the flume with elevation of each ADV instrument, mound size, water depth, and sand bed thickness. Longitudinal (x) and vertical (z) coordinates, and direction of the coordinates are shown. (b) Photo of the piston-type wave maker. The direction of unidirectional currents discharged from the current pump beneath the wave maker is also shown. (c) Photo of the wave absorption pad.

flat bed (Figure 2). The Shields parameter is a non-dimensional shear stress and for our purposes it was only used to show the relative difference in forcing conditions between each experiment. For the interested reader, we define the wave, current, and combined wave current Shields parameters in the Text S1 in Supporting Information S1 of this manuscript. The critical Shields parameter was estimated using the Soulsby and Whitehouse (1997) formula: $\theta_{cr} = \frac{0.3}{1+1.2D_*} + 0.055\left(1 - e^{-0.02D_*}\right)$, where D_* is the dimensionless grain size. For the experimental grain size ($d_{50} = 0.215$ mm), which yields $\theta_{cr} \approx 0.046$. Elevated θ values at the mound top are attributed to flow acceleration and reduced local water depth.

2.3. Morphodynamics

Prior to each experiment the bed level was returned to the same morphology with a Gaussian mound and no bedforms. For the analysis presented, we selected cross-section of 10 cm width from the lidar scan measurements near the centerline of the mound ($y = 0$) that were fairly uniform in the transverse direction. The measurements within that 10 cm band were averaged in the transverse direction to form the quasi-2D morphology used for analyses presented herein (Figure 4a). A smoothed cross-section of the mound morphology at the mound center-line was found by interpolating between ripple troughs (Figure 4b). The mound profile without ripples was considered the local bed over which the ripples were intersecting. The horizontal gradient of the local bed elevation (slope

Table 2
Input Wave and Current Conditions for Each Experiment

Flow condition	Wave height (m)	Wave period (s)	Current velocity (m/s)	# Of runs (duration of each run)
Wave-Only	0.16	1.3	–	9 (6.66 min)
$\theta_w > \theta_c$	0.16	1.3	0.18	9 (5 min)
$\theta_w \sim \theta_c$	0.13	1.2	0.21	9 (5 min)
$\theta_w < \theta_c$	0.11	1.0	0.24	9 (5 min)
Current-Only	–	–	0.29	8 (5 min)

Note. Wave height, period, and current velocity are shown. Number of runs for each experiment are also shown and total duration is equal to the multiplication between number of runs and duration of each run in the table.

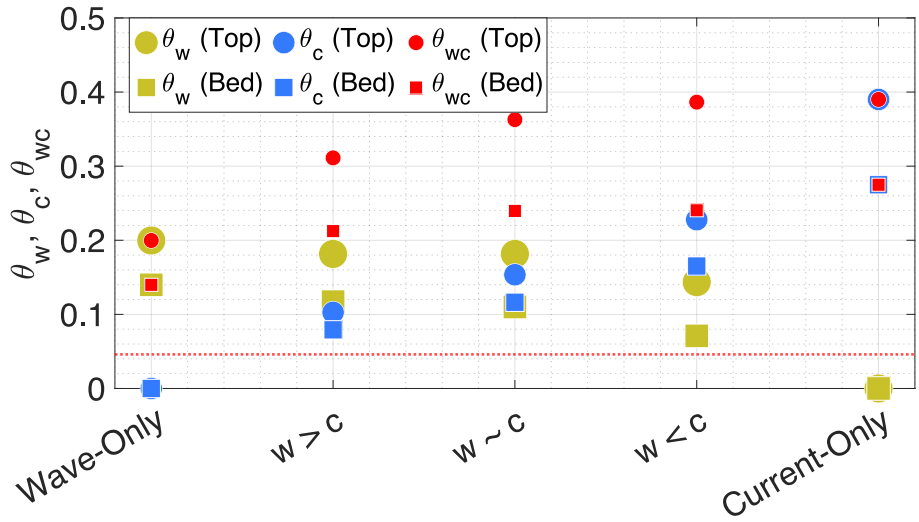

Figure 2. Estimated Shields parameter for wave-induced (θ_w), current-induced (θ_c), and combined wave-current flow-induced (θ_{wc}) shear stress at the mound top (solid circles) and flat bed (solid squares) under five flow conditions. The colors represent wave-only Shields parameter (yellow), current-only Shields parameter (blue), and combined wave–current Shields parameter (red). The red horizontal dashed line indicates the critical Shields parameter for sediment motion ($\theta_{cr} = 0.046$).

between two trough points) was defined as the local bed slope ($\tan\beta$), where β is bed slope angle, expressed in units of degrees (Figure 4b). The smoothed cross-section profile was then subtracted from the original mound profile to leave the ripple signature. The ripple crest and trough points, extracted using a peak-finding method, were used to estimate ripple geometric metrics including height, wavelength, and asymmetry (Figure 4c).

Ripple height (η) was estimated as the vertical elevation between the crest point and the detrended quasi-2D mound trough point (Figure 4c). Ripple wavelength (λ) was estimated as the horizontal distance between two ripple crest points (Figure 4c). The location of the ripple was defined as the x-location of the crest point. Ripple asymmetry was found by taking the ratio between the horizontal length between the ripple trough and ripple crest on the stoss side (a) divided by the horizontal length between the ripple trough and ripple crest on the lee side (b) (Figure 4c). By definition, a/b larger than one indicates a mild stoss slope and a steep lee slope. The ripple asymmetry when the ripple intersects a sloping bed can be predicted through geometrical analysis. This asymmetry, referred to as the slope-induced ripple asymmetry, $(a/b)_{slp}$, is given as a function of η, λ, and local slope

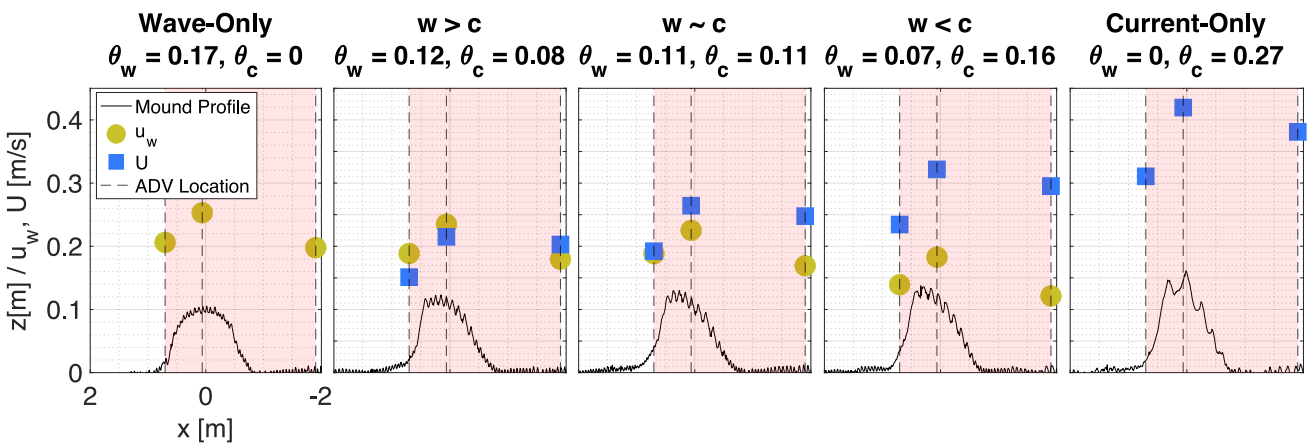

Figure 3. Velocity point measurements along the quasi-2D mound slice for each experiment. Each panel corresponds to a distinct flow condition: wave-only, wave-dominant ($\theta_w > \theta_c$), balanced ($\theta_w \sim \theta_c$), current-dominant ($\theta_w < \theta_c$), and current-only. The mound profile is shown as a black solid line, with red shaded regions indicating the spatial domain used for ripple prediction. Yellow circles and blue squares represent experiment-averaged near-bed wave orbital velocity amplitude (u_w) and depth-averaged current velocity (U), respectively, measured at three Acoustic Doppler Velocimeters locations (dashed vertical lines). Dimensionless Shields parameters (θ_w, θ_c), computed from u_w and U, are shown above each panel to indicate the relative contribution of wave and current-induced shear stress.

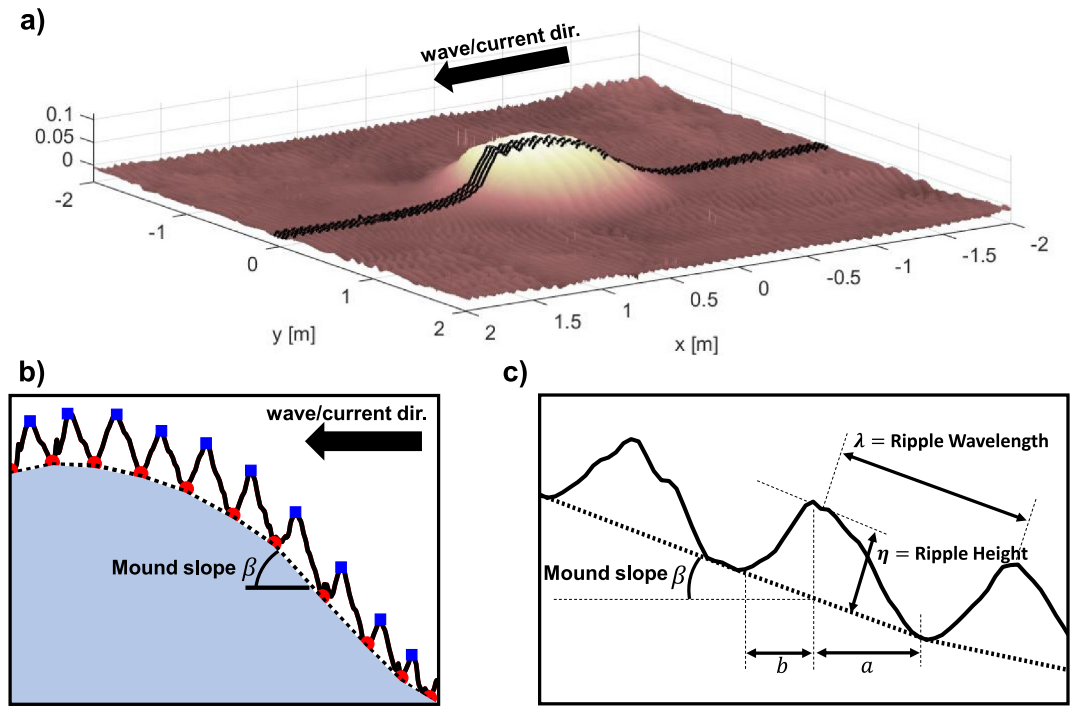

Figure 4. Example of mound and ripple geometry extracted in the wave and current propagation direction. (a) Lidar scan of the bed with the extracted cross-sections near $y = 0$ (black solid lines). (b) Mound profile is removed (dashed line) and ripple crest and trough position are collected. Each ripple crest and trough position is shown by blue square and red circle markers, respectively. The smoothed mound connected with all ripple troughs is shown by the black dashed line. Mound slope angle (β) is defined as the angle between the horizontal axis and the straight line between troughs (dashed line). Wave and current direction is shown by thick solid arrow. (c) Example of ripple on the mound slope (black solid line), with ripple height, wavelength, and horizontal lengths (a-stoss side and b-lee side) to collect slope-induced asymmetry observations ($(a/b)_{obs}$).

angle (β) as follows (see Text S4 in Supporting Information S1 for detailed derivation of slope-induced ripple asymmetry).

$$\left(\frac{a}{b}\right)_{slp} = \frac{2\eta + \lambda \tan\beta}{2\eta - \lambda \tan\beta} \tag{3}$$

3. Experimental Observations

3.1. Quasi-2D Mound Evolution

The overall morphological change of the mound is examined with two lidar scans collected pre- and post-experiment (as seen in Figure 3, black line). In the quasi-2D slice from the post-experiment lidar scan we observed a degree of the asymmetry along the mound that varied as a function of wave to combined wave-current flow velocity ratio. In the wave-only case (without currents), the peak of the Gaussian mound remained centered at $x = 0$. The spreading pattern of sand in the wave-only case was relatively symmetric. In the presence of any magnitude of current, asymmetric spreading toward the shoreward side of the mound was observed. The mound asymmetry became more pronounced as the currents became more dominant.

3.2. Ripple Geometry

We present quasi-2D observations of ripple height, wavelength, and asymmetry investigate ripple geometric variation with respect to varying unidirectional wave-current combinations and bed slope (Figures 5–7). Overall, currents were observed to play a significant role in the growth and shape of ripples toward the top of the mound.

The ripple wavelength and height at the top of the mound increased with current dominance (Figures 5a and 5b; Figures 6b and 6d). Both ripple height and wavelength increased on the wave-maker side of the mound (upslope:

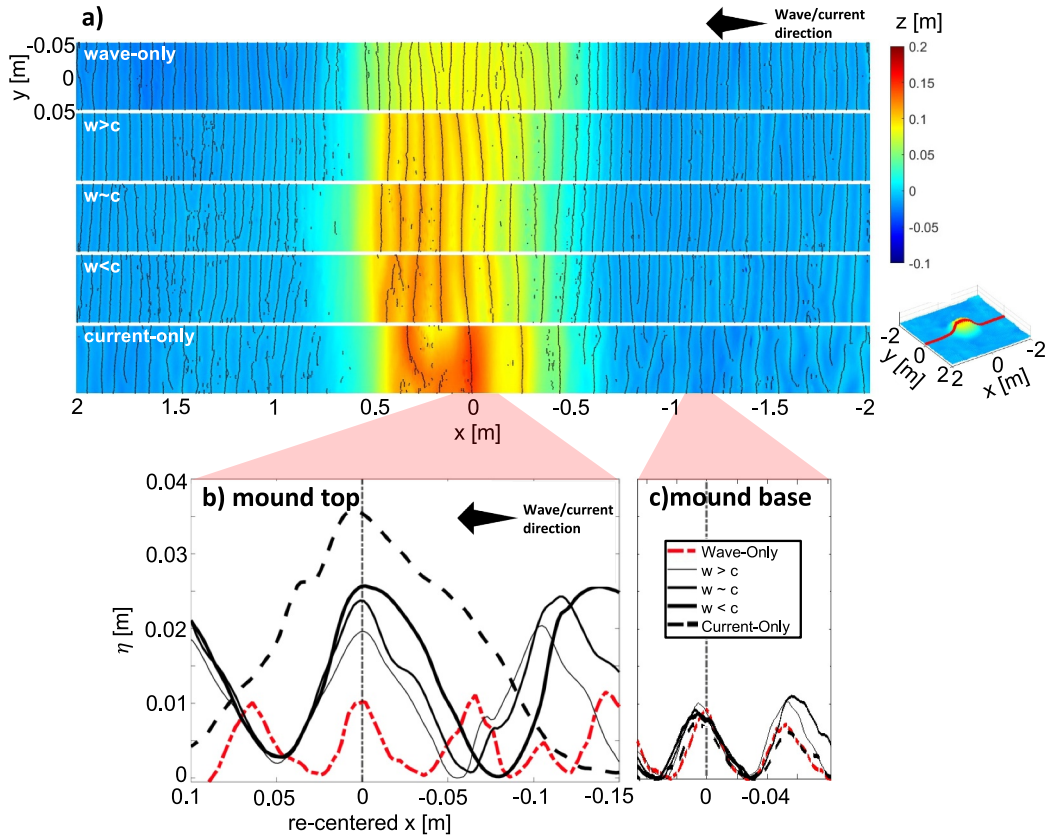

Figure 5. (a) Morphology of the longitudinal quasi-2D mound profile near $y = 0$, overlaid with ripple crest locations shown as thin black solid lines. The label in the upper-left corner indicates the flow condition, and color represents mound elevation. (b) and (c) Representative cross-sectional ripple profiles in the direction of waves and currents at the mound top (b) and base (c). Line styles denote different flow conditions. For clarity and ease of comparison, all ripple profiles in (b) and (c) are re-centered such that the main ripple crest is located at $x = 0$ (vertical dash-dot line), regardless of the original physical location of the ripple to enable direct visual comparison of ripple symmetry and scale relative to the ripple crest. Flow regimes for combined wave–current conditions are categorized as wave-dominant (w>c), balanced (w∼c), and current-dominant (w<c) based on the relative magnitude of wave and current Shields parameters.

$\beta > 0$ in Figures 6a and 6c; x [m] $\in [-1, 0]$ in Figures 7b and 7c), then reached their maximum just before the mound crest (x [m] $\simeq 0$), and subsequently decreased on the mound top and downslope region (downslope: $\beta \leq 0$ in Figures 6a and 6c; x [m] $\in [0, 1]$ in Figures 7b and 7c). The maximum mound slope did not necessarily correspond to the transition point between ripple growth and decay (Figures 6a and 6c; Figures 7b and 7c). The difference in wavelength and height between ripples at the mound top and base varied with the magnitude of the current (Figure 5c). In the wave-only case, there was a 10%–15% increase in ripple wavelength and height at the mound top compared to the mound base (Figures 5b and 5c). For cases with combined waves and currents, the ripple wavelength and height at the mound top were 150%–200% longer than at mound base (Figures 5b and 5c). There was no significant variation in the ripple wavelength or height observed on the flat bed adjacent to the mound regardless of flow condition.

Ripples were observed to be more asymmetric with increasing current dominance (Figure 5b). An asymmetry index was used to assess ripple asymmetry, an index value of one indicates a symmetric ripple. The ripple asymmetry was estimated from observations (Figure 7d) and was also compared to the slope-induced ripple asymmetry (Figures 7e and Equation 3). The observed asymmetry index reached values near 1 for wave-only conditions on the flat bed ($\beta = 0$ in Figures 7d–7i), and the difference between observed and slope-induced asymmetry was close to zero (Figures 7e–7i). On the flat bed in the presence of currents the asymmetry index reached values larger than 1, which indicates a mild stoss side ripple slope and steep lee side ripple slope (Figures 7d-dii–dv). The observed asymmetry index for ripples on the upslope ($\beta > 0$ in Figure 7d) increased until

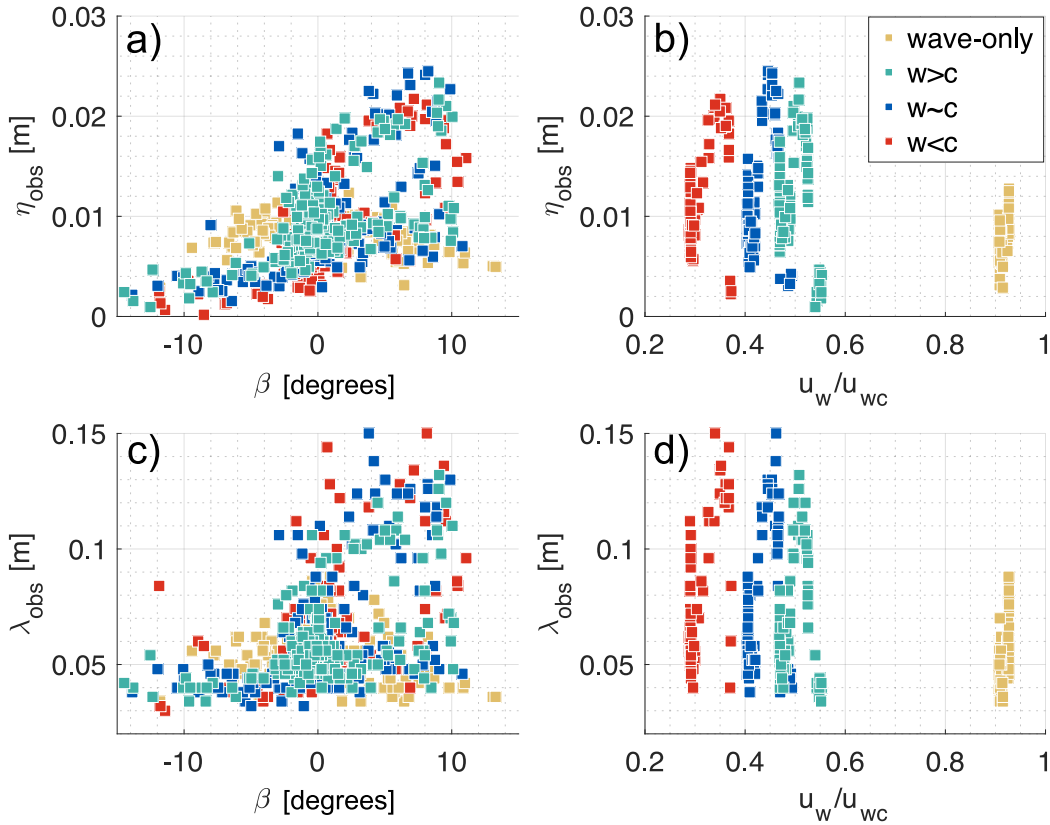

Figure 6. Observed ripple height (η_{obs}, panels (a and b) and wavelength (λ_{obs}, panels (c and d) plotted against local slope angle (β, panels (a and c) and the ratio of wave to combined wave–current velocity (u_w/u_{wc}, panels (b and d). Positive β denotes upslope, and different colors indicate separate experimental conditions Current-only condition ripple is not included due to the large variability. Flow regimes for combined wave–current conditions are categorized as wave-dominant (w>c), balanced (w~c), and current-dominant (w<c) based on the relative magnitude of wave and current Shields parameters.

the ripple reached the top of the mound. The asymmetry index reached its maximum on the upslope, and the maximum observed asymmetry increased with respect to current dominance (about 2 for w>c to about 3 for current-only in Figures 7d-dii–dv). Combined wave-current and current driven ripples on the upslope of the mound had an observed asymmetry that was smaller than the slope-induced asymmetry (Figures 7e-eii–ev). The ripple asymmetry index decreased below one on the downslope side of the mound ($\beta < 0$), which indicates a steep stoss side ripple slope and mild lee side ripple slope (Figure 7d). In the combined flow and current dominant conditions the ripples on the downslope side of the mound became unstable and avalanched because of the steep combined mound and ripple slope. After ripple avalanching, the ripple asymmetry index reached 1 again on the flat bed shoreward of the mound ($+x$). Overall, the observed asymmetry was larger than the slope-induced asymmetry with increasing current dominance (Figures 7e-eii–ev). The observed discrepancy between the predicted and slope-induced asymmetry using Equation 3 indicates that the slope-induced asymmetry under combined flow must be corrected to account for the effects of combined flow.

4. Equilibrium Ripple Predictors

4.1. Existing Ripple Predictors for Combined Wave-Current Flows

We observed that ripple geometry (i.e., height, wavelength, asymmetry) varied with bed slope and wave to combined wave-current flow velocity ratio (Figures 5–7). Our objective in this section is to determine if an existing ripple geometry predictor can accurately estimate ripple geometry on a sloping bed. We assessed four equilibrium ripple geometry predictors that were developed for combined wave-current flows over flat beds (Khelifa & Ouellet, 2000; Nielsen, 1981; Soulsby et al., 2012; Tanaka & Dang, 1996). Table 3 and Text S3 in Supporting Information S1 provide details on the formulation of each ripple predictor. We assumed that the

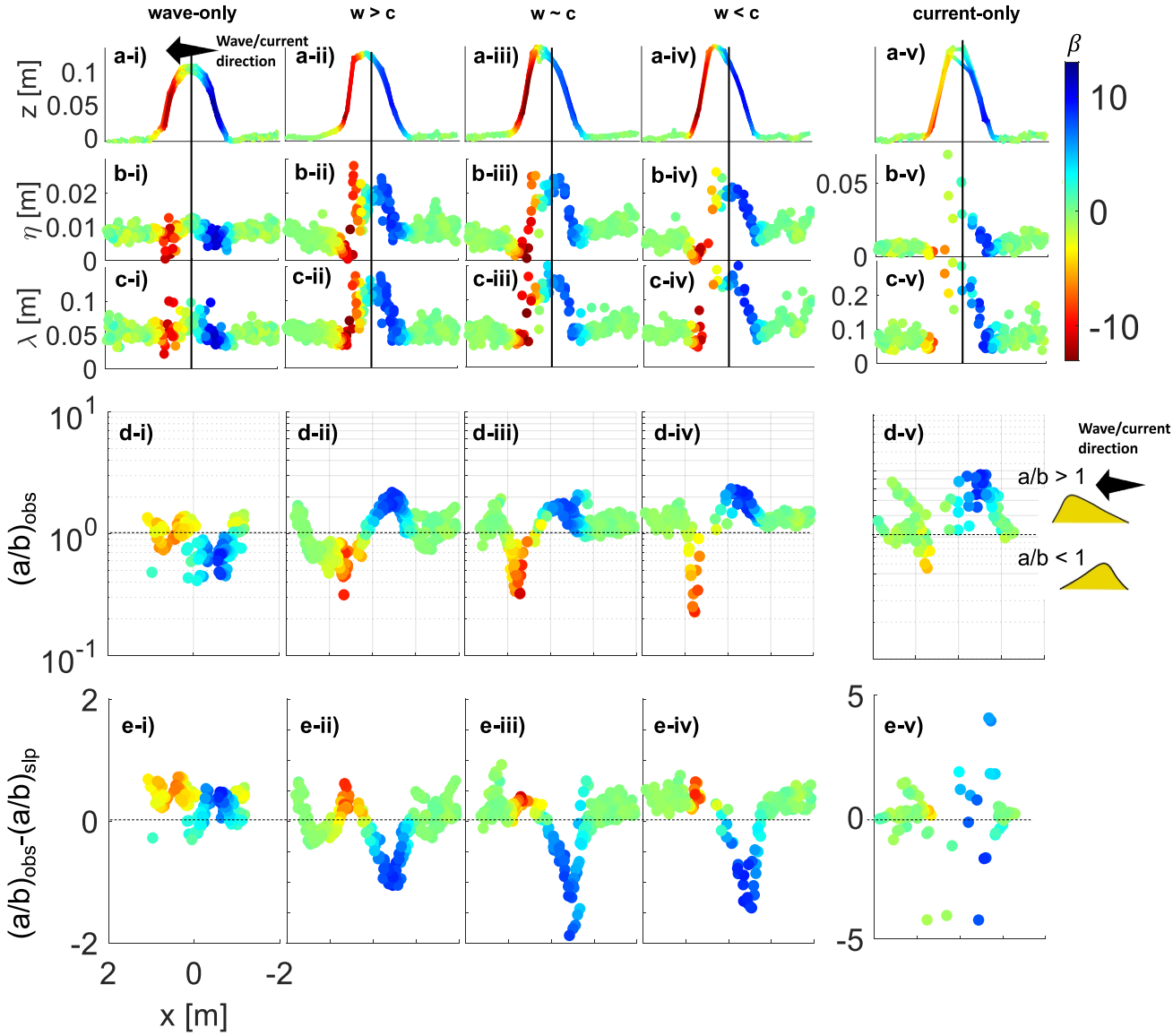

Figure 7. Ripple geometry at $y = 0$ along the direction of wave propagation and current flow. (a) Reference mound shape near $y = 0$. (b) Ripple height and (c) ripple wavelength. (d) Asymmetry index (a/b) of ripples with different x-location. Reference schematics of ripple asymmetry index are shown to the right of panel d–v. (e) Asymmetry difference between observation ($(a/b)_{obs}$) and slope-induced asymmetry ($(a/b)_{slp}$). The slope-induced asymmetry is estimated by Equation 3; color of scatter in panel (a, b, c, d, and e) represents slope angle of mound excluding ripple angle on which ripples intersected (β). If the flow of waves or currents goes up from the flat bed to the top of the mound, the slope is defined as upslope (blue), and vice versa for downslope (red). Flow regimes for combined wave–current conditions are categorized as wave-dominant (w>c), balanced (w∼c), and current-dominant (w<c) based on the relative magnitude of wave and current Shields parameters.

ripples we observed on the mound were in equilibrium with the flow conditions. The chosen predictors use hydrodynamic metrics as inputs (u_w, U, $d_0 = u_w T/\pi$, $A = d_0/2$, θ_w, θ_c).

4.2. Evaluation Metrics

To evaluate the performance of each predictor, normalized root-mean square error (nRMSE) and Index of Agreement (I_a) were adopted, which are given by.

$$nRMSE = \sqrt{\frac{\Sigma(P-O)^2}{\Sigma O^2}} \tag{4}$$

Table 3
Equilibrium Ripple Geometry Predictors for Combined Wave-Current Flows

Ripple predictor	Abbreviation	Input parameters
Corrected Nielsen (1981)	Ni81	u_w, U, A, h, d_{50}
Tanaka and Dang (1996)	TD96	u_w, U, d_0, d_{50}
Khelifa and Ouellet (2000)	KhO00	u_{wc}, d_{50}
Soulsby et al. (2012)	So12	A, d_{50}, θ_w, θ_c

Note. uw u_w is near-bed wave orbital velocity amplitude, U is mean current velocity, A is semi-orbital excursion ($=u_wT/\pi$), h is water depth, d_{50} is median grain size, d_0 is orbital excursion ($=2A$), u_{wc} is combined wave-current flow velocity, θ_w is wave Shields parameter, and θ_c is current Shields Parameter.

$$I_a = 1 - \frac{\Sigma(P-O)^2}{\Sigma\left(|O-\overline{O}| + |P-\overline{O}|\right)^2} \quad (5)$$

where P is prediction, and O is observation. If nRMSE is close to 0, the prediction is close to the observation, and if I_a is close to 1, the prediction versus observation is close to a 1:1 relation.

4.3. Evaluation of Existing Ripple Geometry Predictors

We evaluated the four chosen combined wave-current ripple geometry predictors using nRMSE and I_a on a sloping bed and on a flat bed (Figure 8).For the wave-only ripple predictions, predictors showed moderate skill in predicting ripple height and wavelength (I_a = 0.55–0.68 in Figures 8e and 8g). When only the ripples on the flat bed were considered, the predictor showed better performance for TD96, KhO00, and So12 (I_a = 0.75–0.85 in Figures 8f and 8h). Overall the TD96 predictor (Tanaka & Dang, 1996) performed the best for prediction of ripple height and wavelength in combined flow conditions on the flat bed (Figure 8). For TD96, the nRMSE was the lowest and I_a was the highest for all tested conditions (Figure 8). Generally, KhO00, So12, and Ni81 performed variably for prediction of the flat bed ripple geometry dependent on combined wave-current condition, and overall much poorer than TD96.

When we used any of the ripple predictors for ripples on the sloping bed, the performance decreased for all models and notably for the TD96 predictor (Figure 8), even though the TD96 still had the highest overall skill of all tested predictors. The decrease in skill of the predictors for ripple geometry on a sloped bed suggests that the existing predictors are not suitable for predicting ripple height and wavelength on a sloped bed.

Additionally, the performance of the existing ripple predictors decreased with increasing current dominance. For example, prediction of ripple height (wavelength), I_a was observed to decrease by 80% (70%) from the wave-only case to the w<c case (Figures 8e and 8g). The decrease in model skill with increased current (combined with

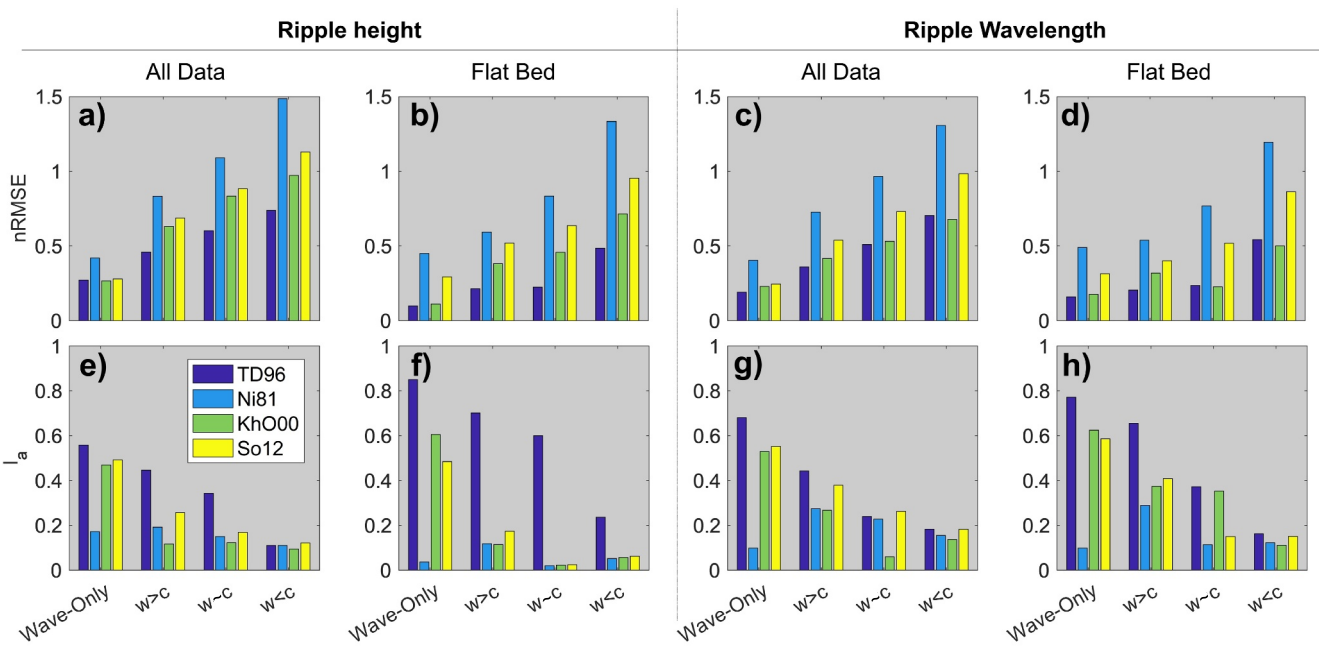

Figure 8. Summary of performance of combined wave-current ripple predictors with normalized root-mean square error (nRMSE: (a, b, c, d) and index of agreement (I_a: (e, f, g, h) for ripple height (a, b, e, f) and ripple wavelength (c, d, g, h). Each of the four columns of bars within a single panel show different combined flow conditions, and each column has four bars, one for each ripple predictor shown by different colors corresponding to Table 3. Current-only cases are not included since there are no predictors evaluated for current-only conditions. Flow regimes for combined wave–current conditions are categorized as wave-dominant (w>c), balanced (w~c), and current-dominant (w<c) based on the relative magnitude of wave and current Shields parameters.

waves) indicates that the wave to combined wave-current flow velocity ratio and bed slope are interdependent, and for accurate prediction of ripple geometry the effect of the wave-current velocity ratio and bed slope must be considered collectively.

4.4. Correction of Ripple Geometry Predictor for Bed Slope and Wave to Combined Wave-Current Flow Velocity Ratio

We propose an adjustment to the ripple geometry predictors to account for changes in bedload transport as a function of bed slope. The estimated bedload transport on a flat bed can be adjusted for transport on a sloped bed with a slope factor (S_f) that is a function of the angle of repose and the local bed slope angle (Bagnold, 1956; Bailard & Inman, 1981; Damgaard et al., 1997; Hardisty & Whitehouse, 1988). This factor (S_f) represents the ratio between the shear force for bedload transport on a sloping bed and for bedload transport on a flat bed (Bagnold, 1956), and is given by

$$S_f = \frac{F_{D,flat}}{F_{D,slp}} = \frac{\tan\alpha_c(s-1)\rho g V_s}{\cos\beta(\tan\alpha_c - \tan\beta)(s-1)\rho g V_s} = \frac{\tan\alpha_c}{\cos\beta(\tan\alpha_c - \tan\beta)} \tag{6}$$

where $F_{D,flat}$ is the shear force on a flat bed, $F_{D,slp}$ is shear force on a sloping bed, ρ is density of water, V_s is volume of a sand grain, α_c is the angle of repose, and β is the bed slope angle. Hardisty and Whitehouse (1988) found that the slope factor can be simplified to the following form, which has better agreement with their bedload transport experimental data,

$$S_f = \left[\frac{\tan\alpha_c}{\tan\alpha_c - \tan\beta}\right]. \tag{7}$$

Hardisty and Whitehouse (1988) added a power term (p) on the S_f, which the power of S_f ($= (S_f)^p$) is the corrector of slope effect on the bedload transport. The p was determined empirically ($p = 7$ for Hardisty and Whitehouse (1988)).

We implemented a modified slope factor into the best performing ripple geometry predictor (TD96) based on mound bed slope (Equation 7) and the wave to combined wave-current flow velocity ratio. Since we observed that both slope and wave-current velocity ratio influence ripple height, wavelength, and asymmetry, we adjusted the power term p in Equation 7 to be a function of the wave to combined wave-current flow velocity ratio ($p = f(u_w/u_{wc})$).

The proposed corrections to the predictor formulations for ripple height (η_{corr}) and wavelength (λ_{corr}) to include the influence of slope and the wave to combined wave-current flow velocity ratio are as follows:

$$\eta_{corr} = \frac{\eta_{model}}{(a_1 S_f)^{pK}} - b_1 K \tag{8}$$

$$\lambda_{corr} = \frac{\lambda_{model}}{(a_2 S_f)^{pK}} - b_2 K \tag{9}$$

where η_{model} and λ_{model} are the ripple height and wavelength estimated using an un-corrected ripple geometry predictor. S_f is the slope correction defined as Equation 7 with the angle of repose set to 31°. p and K are the previously defined power term, where $p = u_w/u_{wc}$, and K is hyperbolic tangent function for the local slope angle ($= (1 - \exp 2|\beta|^3)/(1 + \exp 2|\beta|^3)$). When the slope angle is $\beta = 0°$ on the flat bed, the K in Equations 8 and 9 becomes zero, and the corrected predictor becomes equivalent to the original predictor used for both the ripple height and wavelength predictions, so $\eta_{corr} = \eta_{model}$ and $\lambda_{corr} = \lambda_{model}$. $a1, a2, b1, b2$ are empirically derived coefficients for predictor tuning; calibrated to our data set $a1 = 0.343 \pm 0.0053$, $b1 = 0.0084 \pm 0.0013$ for ripple height and $a2 = 0.3449 \pm 0.0065$, $b2 = 0.0479 \pm 0.0089$ for ripple wavelength. To determine the coefficients, bootstrap resampling was used (Efron, 1982). To perform the fit, 70% of the total data were randomly chosen, then the performance was evaluated with the remaining 30% of data. The bootstrap resampling and validation was carried out 500 times and mean and standard deviation from the 500 coefficients were those given

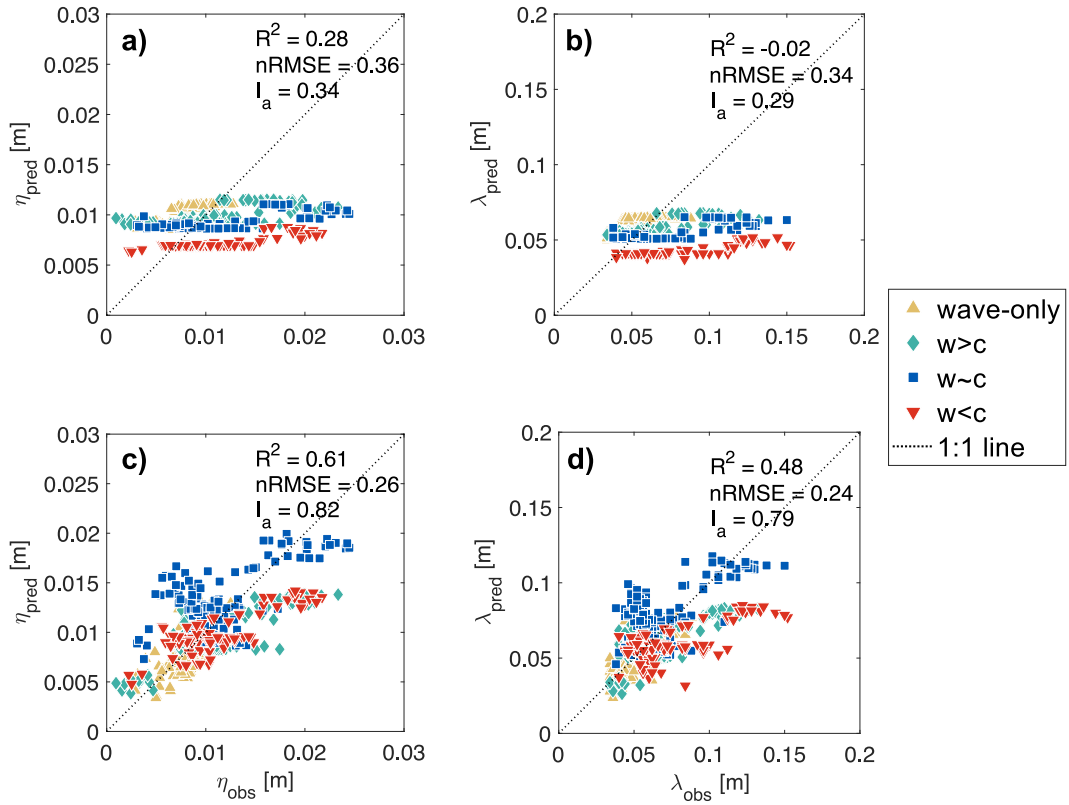

Figure 9. Comparison between ripple geometry observations and predictor results for both the original ripple predictor (TD96–a, b) and the slope and combined flow corrected predictor (c, d) are shown. Point shapes and colors vary by varying wave to combined wave-current flow velocity ratio. Predictor performance is shown as a coefficient of determination (R^2), normalized root-mean square error, and index of agreement (I_a) for both $\eta_{mod} \rightarrow \eta_{corr}$ and $\lambda_{mod} \rightarrow \lambda_{corr}$. Current-only cases are not shown because we focused this work on wave and combined flow conditions. Flow regimes for combined wave–current conditions are categorized as wave-dominant (w>c), balanced (w~c), and current-dominant (w<c) based on the relative magnitude of wave and current Shields parameters.

as $a1$, $b1$, $a2$, and $b2$. The standard deviation of each coefficient is shown by the $+/-$ after each mean coefficient value.

We selected the TD96 ripple predictor by Tanaka and Dang (1996) to correct as it performed the best (highest $I_a = 0.75 - 0.85$ and lowest nRMSE $= 0.10 - 0.15$) on regions of the flat bed (Figures 8b–8d and 8f, h) in combined wave-current and wave-only conditions in this study. The proposed correction factors (Equations 8 and 9) are applied to the original predictor output by TD96 (η_{pred}, λ_{pred} in Figures 9a and 9b) to obtain the corrected ripple geometry (η_{pred}, λ_{pred} in Figures 9c and 9d). We observed that for the corrected predictors, all three performance indices improved (R^2 improved by more than 100%, nRMSE improved by 27%–29%, and I_a improved by 145%–168%) for predictions of ripple height and wavelength on the sloping bed (Figure 9).

4.5. Correction of Ripple Asymmetry Predictor

Our observations revealed a difference in the stoss side and lee side lengths of ripples (i.e., ripple asymmetry) that cannot be explained solely by the geometry of symmetric ripples intersecting an upslope or downslope (Figures 7d and 7e). This slope-induced asymmetry, which only accounts for the local slope, showed a discrepancy when compared with the observed ripple asymmetry (Figure 7e). The discrepancy between the observed and slope-induced asymmetry was observed to be a function of the wave to combined wave-current flow velocity ratio. We applied the wave to combined wave-current flow velocity ratio correction to the slope-induced asymmetry, given by

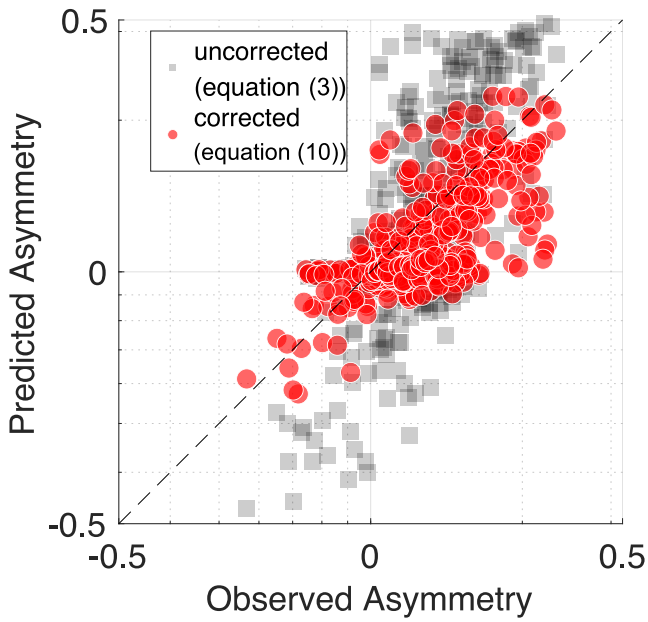

Figure 10. Log-scale of observed ripple asymmetry ($(a/b)_{obs}$-Observed Asymmetry) plotted against the log-scale of corrected (red circles) and uncorrected (gray squares) slope-induced asymmetry (Predicted Asymmetry). Slope-induced asymmetry ($(a/b)_{slp}$) is estimated with Equation 3 using observed ripple heights, wavelengths, and slope angle, and the corrected slope-induced asymmetry uses the wave to combined wave-current flow velocity ratio to correct the slope-induced asymmetry as shown in Equation 10. Index of agreement and root-mean square error are normalized root-mean square error (nRMSE) = 0.47, $I_a = 0.77$ for uncorrected, and nRMSE = 0.19, $I_a = 0.83$ for corrected.

$$(a/b)_{corr} = (a/b)_{slp}^{(1-p)}, \tag{10}$$

where $(a/b)_{slp}$ is the slope-induced asymmetry from Equation 3, and $p = u_w/u_{wc}$.

After correction, using Equation 10, the corrected model reduced the discrepancy between the observed ripple asymmetry and the asymmetry predicted using slope alone, as indicated by a reduction in the root-mean-square error for the corrected model. Additionally, the model showed an improved index of agreement (Figure 10). The correction for combined wave-current flow enhances the slope-induced asymmetry predictor's ability to account for slope effects.

5. Discussion

Figure 11 schematically summarizes the evolution and decay of the ripple geometry observed under varying wave-current and slope conditions. The focus of the discussion is on interpreting the mechanisms that control ripple variability in wave-current conditions and on a changing bed slope, their implications, and limitations of this study.

5.1. Adjusting Bedform Characteristics for Slope Under Combined Wave-Current Flows

It is well known that gradients in bed level affect bedload sediment transport (Apsley & Stansby, 2008; Bagnold, 1956; Damgaard et al., 1997; Lee et al., 2023). Bedload transport is related to bedform migration and so it is not surprising to find spatial variation in ripples over the quasi-2D mound cross section. Our observations showed that the growth or decay of ripples was related to the slope angle of the mound (Figure 7). Additionally, with increased current strength on the sloped bathymetry, larger and more asymmetric ripples formed (Figure 10). Damgaard et al. (2003) also reported that

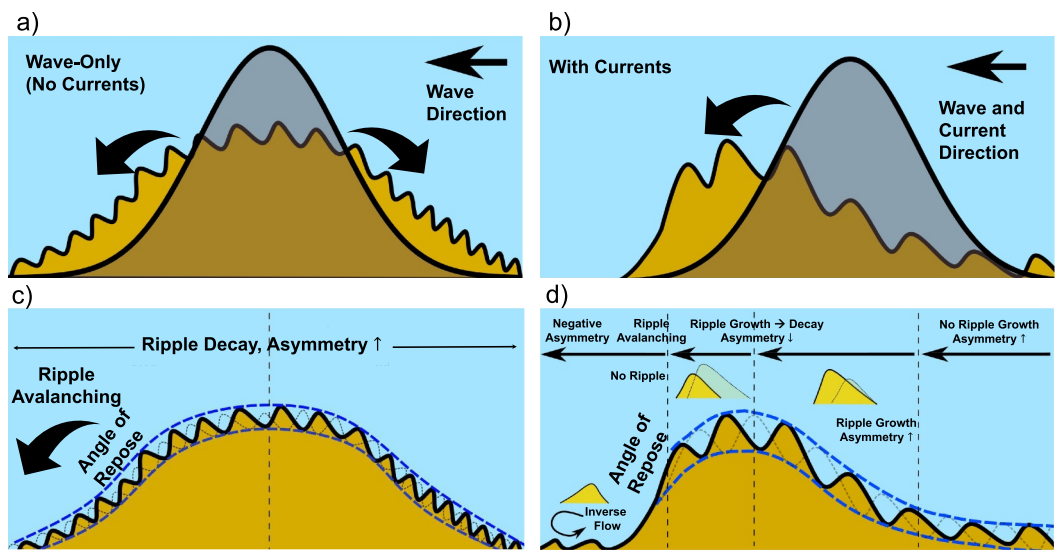

Figure 11. Schematic showing ripple geometry as a function of flow condition and position on the mound. (a) Mound spreading under wave-only condition with (c) decaying of ripples. (b) Mound spreading under combined wave-current flows and (d) ripple evolution on sloped bed. Gray area in (a) and (b) shows initial mound, yellow area shows spreading mound. Blue dashed lines in (c) and (d) show envelope between ripple crest and trough.

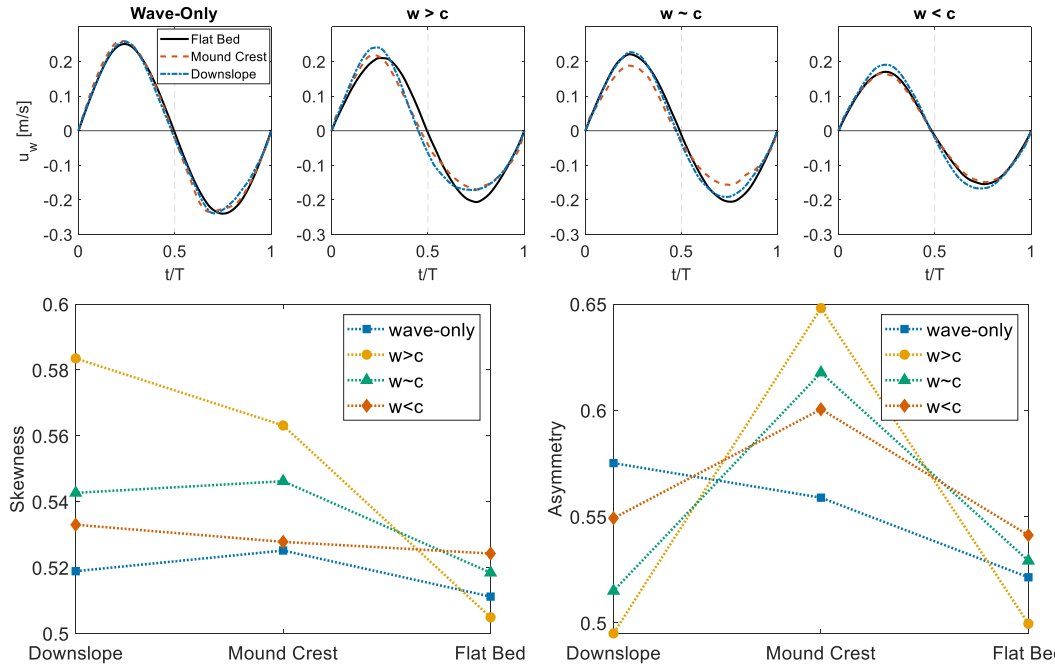

Figure 12. Phase-averaged wave orbital velocity (u_w) for all conditions (top). Time-domain skewness and asymmetry of phase-averaged orbital velocity across three Acoustic Doppler Velocimeters locations (downslope, mound crest, flat bed) under four flow conditions (bottom). Flow regimes for combined wave–current conditions are categorized as wave-dominant (w>c), balanced (w∼c), and current-dominant (w<c) based on the relative magnitude of wave and current Shields parameters.

on an upslope with a base angle of 10° ripple volume increased with current strength, and reported decay in volume on downslopes (Damgaard et al., 1997).

When we examined the ripple geometry under the presence of increased levels of current dominance, we noticed that ripples tend to have a gentle stoss side slope and a steep lee slope (Figure 7d). When the asymmetric ripples were positioned on the upslope of the mound, the stoss side slope of the ripple increased due to the addition of the mound base slope angle and the stoss side slope angle of the ripple. On the other hand, the bed slope was reduced from the mound base slope due to the addition of the ripple lee-side angle, which reduced the likelihood of slope avalanching on the upslope of the mound. Consequently, more sand volume can be stored in the ripple within current dominant flows with or without waves on the bathymetric upslope with respect to current direction. This phenomenon highlights the discrepancy between observed and slope-induced asymmetry described by Equation 3, which is attributed to the lack of consideration for the combined wave-current flow effect. The discrepancy was corrected by incorporating the ratio of wave to combined wave-current flow velocity (Figure 10). Therefore, in combined flow conditions, we found that existing ripple geometry predictors that primarily consider local hydrodynamics on a flat bed, were not able to accurately capture the observed variations in ripple geometry on a sloped bed, and it is essential to simultaneously consider local slope and the wave to combined wave-current flow velocity ratio to accurately predict the geometry of ripples.

In this study, the direction of waves and currents aligned along the slope (longitudinal direction). However, if the waves and currents were on a transverse slope, a slope factor for bedload transport correction as a function of transverse slope angle may need to be considered (Baar et al., 2018; Ikeda, 1982).

5.2. Effect of Velocity Skewness and Asymmetry

Our phase-averaged velocity measurements reveal distortion of orbital velocity through the mound, particularly under wave–current interaction (Figure 12). The spatial evolution of orbital velocity shape is captured by the skewness parameter ($R_u = u_{max}/(u_{max} - u_{min})$, where u_{max} and u_{min} are maximum and minimum wave orbital velocity, respectively), which quantifies the asymmetry in velocity magnitude (Ribberink & Al-Salem, 1994), and

the asymmetry parameter ($R_a = a_{max}/(a_{max} - a_{min})$, where a_{max} and a_{min} are maximum and minimum acceleration of wave orbital velocity, respectively), which characterizes steepness asymmetry (Watanabe & Sato, 2005).

Under wave-dominant conditions (w>c), both R_u and R_a exhibit pronounced peaks at the mound crest, indicating enhanced nonlinear wave transformation due to flow convergence and shoaling, which can drive sediment transport in the wave direction. The elevated R_u near the downslope suggests intensified onshore-directed velocity excursions, while the peak in R_a at the crest corresponds to steeper front-face slopes and more abrupt accelerations of the waves. In contrast, wave-only and current-dominant (w<c) conditions show relatively symmetric waveforms with lower and more spatially uniform skewness and asymmetry values.

These results support the interpretation that wave–current interactions and local topographic effects amplify waveform nonlinearity, which in turn modulates the phase and intensity of near-bed shear stresses (Salimi-Tarazouj et al., 2024; Wang & Yuan, 2020). Increased skewness and asymmetry promote stronger and more focused bottom stresses during specific parts of the wave cycle, potentially enhancing sediment transport on the stoss side of the mound and causing lee-side avalanching. This mechanism aligns with the observed increase in ripple wavelength and asymmetry near the upslope of the mound under wave-dominant forcing, demonstrating that there is influence between the hydrodynamic waveform shape and ripple geometry. Our study was limited in observations of flow hydrodynamics to point source measurements in the direction of the defined x-direction over the mound; however, a future direction of work could be to investigate the influence of near-bed velocity skewness and asymmetry on 3D bathymetries.

5.3. Contextualization of This Study

Multiple scales of bedforms can coexist due to flow events with different timescales (Jones & Traykovski, 2019). Such multiscale bedforms are common in nature, for example as smaller bedforms such as ripples can form due to disequilibrium superposition over top of pre-existing large-scale bedforms or bathymetry (e.g., dunes, sandbars or coastal nourishments). We examined ripples on top of a three dimensional sandy mound. In our study, the 1.5 m diameter and 0.2 m in height sand mound represented a pre-existing large-scale feature. We observed ripples with wavelengths of $0.05 - 0.2$ m and heights of $0.01 - 0.02$ m on the mound under the influence of waves and currents. The ripples in reference to the mound correspond to approximately a 1/30–1/10 geometric scale. The presence of the larger scale feature is shown to be important because the combined slope of both morphologic scales will influence transport and may reach the angle of repose and reach avalanching as shown in Figure 11. A similar difference in geometric scale between multiple bedforms was observed in the field by Jones and Traykovski (2019). They observed megaripples with heights of 0.1 m and wavelengths of 1 m, superimposed on dunes with heights of 2 m and wavelengths of 100 m. This represents a geometric scale of approximately 1/50–1/20 between the superimposed megaripples and the height of dunes. The 100 m wavelength dune of Jones and Traykovski (2019) had a relatively gentle slope of only 0.1 (approximately 6–7° on the stoss side), while the sand mound in our study had a steeper slope, reaching a maximum of 15°. The Froude number ($Fr = V/\sqrt{gh}$, where V is the combined wave-current velocity, g is the gravitational acceleration, and h is the local depth) for this study indicates subcritical flow for all combined wave-current cases ($Fr = 0.20 - 0.35$) and wave-only cases ($Fr = 0.10 - 0.15$). This is consistent with the expected ripple formation for the median grain size of 0.215 mm according to bedform classification diagrams (Ashley, 1990). Therefore, when a large-scale bedform or nourished profile is subject to subcritical flow and within the ripple formation regime, ripples with a height of at least 1/20 of the geometric scale may be observed under wave-current flow conditions (Ashley, 1990). The Froude number is similar to those from the field observations of Jones and Traykovski (2019) ($Fr < 0.1$). However, the exact size of the ripples will vary depending on the local bed slope and the wave to combined wave-current flow velocity ratio.

Both the contextualization of the geometric scale and Froude scaling for the multiscale bedforms in this study (small-scale ripples and sandy mound) compared with scale from Jones and Traykovski (2019) demonstrates that the observed effect of bed slope on ripple geometry is relevant to field conditions and could occur in many systems where bedforms are superimposed on larger sloped features (e.g., megaripples, sand waves).

5.4. Implications for Theoretical Frameworks

The observed variations in ripple geometry over a sloped bed under combined wave–current flows can be further contextualized through the bedform instability theory. Several theoretical analyses have demonstrated how flow

instabilities, sediment transport, and feedback mechanisms give rise to self-organized bedforms in various hydrodynamic regimes, especially for current-driven bedforms and sand waves (Colombini, 2004; Colombini & Stocchino, 2008; Dey & Ali, 2020; Dey et al., 2022, 2024).

While our study primarily focused on empirical observations and data-driven corrections for ripple geometry, the spatial variability we observed, particularly the asymmetric ripple growth, decay, and migration, aligns with predictions from these theoretical frameworks when extended to inclined beds and oscillatory or combined forcing. For example, the suppression or enhancement of ripple growth due to local slope effects and wave–current ratio could be interpreted as modulation of the growth rate in the linear stability analysis. Additionally, the downslope decay and avalanche-like behavior observed in our experiments may correspond to saturation or nonlinear equilibration regimes predicted by such models.

Future work could leverage these instability models (Colombini, 2004; Colombini & Stocchino, 2008; Dey & Ali, 2020; Dey et al., 2022, 2024) to extend our empirical corrections into a unified theoretical prediction framework for ripple dynamics on sloped beds under combined flows. Incorporating both linear and weakly nonlinear analyses in such systems would be especially beneficial for understanding transitions between ripple formation, growth, and decay across different slope and forcing regimes.

5.5. Application to Morphodynamic Models

The ripple geometry predictors used in this study were originally formulated to estimate bed roughness on a flat bed (Brakenhoff, Kleinhans, et al., 2020; Elias & Hansen, 2013; Herrling & Winter 2014; Lenstra et al., 2019; Tonnon et al., 2007). However, when dealing with large-scale morphological features with slopes, such as nourished sand placement, the bed slope angle cannot be disregarded due to its significant impact on ripple geometry and corresponding sediment flux. Based on our corrected ripple predictor, a change in slope of 10° alone can result in 60%–100% larger ripples. The direct use of the proposed correction to the Tanaka and Dang (1996) predictor using a modified slope factor that also considers the influence of the wave to combined wave-current flow velocity ratio, could lead to improved predictions of ripple height and wavelength on a sloping bed (between ±10°) in simulated combined wave-current conditions. We anticipate that when the predictor is applied in morphological change modeling frameworks, it will improve estimates of boundary layer hydrodynamics and circulation.

5.6. Limitations and Future Work

In this study, all experiments were conducted with a single sediment grain size (d_{50} = 0.215 mm). Although the ripple predictor developed in this study builds on the grain-size–dependent formulation by Tanaka and Dang (1996), we have not tested the variation of the grain size. Extending the current predictor framework to cover a wider range of sediment sizes represents an important direction for future validation and model generalization.

Additionally, the experiment was conducted in a quasi-two-dimensional mound, where wave and current directions were aligned. In natural environments, however, waves and currents often intersect at oblique angles or vary in direction, and the morphologic features are usually three-dimensional, introducing three-dimensional ripple responses. Our predictor currently assumes a longitudinal slope configuration aligned with the primary flow direction. If currents were to approach a sloped bed at an oblique angle, lateral sediment transport and ripple alignment could be substantially altered. Future research should investigate ripple formation under multi-directional forcing and develop correction factors that incorporate transverse slope effects, potentially extending frameworks proposed by Ikeda (1982) and Baar et al. (2018).

6. Conclusion

We presented detailed observations of ripple geometry combinations of co-aligned waves and currents on a quasi-2D sand mound cross section. When monochromatic waves propagate without currents, the height and wavelength of the ripples were a function of mound elevation and local slope. When both waves and currents were present, the height and wavelength of the ripples increased as a function of local slope and the wave to combined wave-current flow velocity ratio only on the upslope of the mound. The growth of the ripples ceased at the top of the mound, and the ripples reduced in size and steepness until the ripple slope reached the angle of repose near the

shoreward side of the mound, which triggered avalanching, leading to sediment deposition, and very small or no ripples. Overall, we showed that combined flows on a sloped bed significantly influence ripple wavelength, height, and asymmetry.

We then proposed an improvement to an existing ripple geometry predictor to include the interdependent influence of bed slope and combined wave-current flows. Existing ripple geometry predictors for combined wave-current flow conditions performed poorly on the sloped bathymetry. The combined wave-current ripple predictor by Tanaka and Dang (1996) performed the best of the models tested on a flat bed in our experiment. Our proposed correction for combined wave current ripple geometry predictors for bed slope in a range of wave to combined wave-current flow velocity ratios improves the prediction of roughness amplitude and wavelength for the tested Tanaka and Dang (1996) model. Next steps could include implementing and testing the proposed interdependent bed slope and combined wave-current correction factor for ripple geometry prediction into process-based coastal circulation models and coastal morphologic change models to assess how the proposed modifications may improve process based model skill.

Data Availability Statement

The processed ripple geometry and velocity data in the study are available from Lee (2024).

Acknowledgments
The MODEX project was supported by the European Community's Horizon 2020 Programme through the Grant to the budget of the Integrated Infrastructure Initiative Hydralab+, Contract no. 654110. We thank the University of Hull Hydralab + Total Environment Simulator staff, including Stuart McLelland, Brendan Murphy, Hannah Williams and Laura Jordan for their guidance during experiment setup and testing. We also thank the PADI Foundation (11310) for partial funding of participation in the experiments for S-BL and MW. MdS and JH were financed by the Dutch NWO Domain Applied and Engineering Sciences under project code 15058. We also thank Hester Kleinhans-van de Kasteele, who helped derive the slope-induced asymmetry relation. We also thank two anonymous reviewers for their constructive comments to improve the quality of the paper.

References

Apsley, D. D., & Stansby, P. K. (2008). Bed-load sediment transport on large slopes: Model formulation and implementation within a rans solver. *Journal of Hydraulic Engineering*, *134*(10), 1440–1451. https://doi.org/10.1061/(asce)0733-9429(2008)134:10(1440)

Ashley, G. M. (1990). Classification of large-scale subaqueous bedforms; a new look at an old problem. *Journal of Sedimentary Research*, *60*(1), 160–172. https://doi.org/10.2110/jsr.60.160

Baar, A. W., de Smit, J., Uijttewaal, W. S., & Kleinhans, M. G. (2018). Sediment transport of fine sand to fine gravel on transverse bed slopes in rotating annular flume experiments. *Water Resources Research*, *54*(1), 19–45. https://doi.org/10.1002/2017wr020604

Bagnold, R. A. (1956). The flow of cohesionless grains in fluids. *Philosophical Transactions of the Royal Society of London - Series A: Mathematical and Physical Sciences*, *249*(964), 235–297. https://doi.org/10.1098/rsta.1956.0020

Bailard, J. A., & Inman, D. L. (1981). An energetics bedload model for a plane sloping beach: Local transport. *Journal of Geophysical Research*, *86*(C3), 2035–2043. https://doi.org/10.1029/jc086ic03p02035

Brakenhoff, L., Kleinhans, M., Ruessink, G., & vander Vegt, M. (2020a). Spatio-temporal characteristics of small-scale wave–current ripples on the ameland ebb-tidal Delta. *Earth Surface Processes and Landforms*, *45*(5), 1248–1261. https://doi.org/10.1002/esp.4802

Brakenhoff, L., Schrijvershof, R., Van Der Werf, J., Grasmeijer, B., Ruessink, G., & Van Der Vegt, M. (2020b). From ripples to large-scale sand transport: The effects of bedform-related roughness on hydrodynamics and sediment transport patterns in delft3d. *Journal of Marine Science and Engineering*, *8*(11), 892. https://doi.org/10.3390/jmse8110892

Cataño-Lopera, Y. A., & García, M. H. (2006). Geometry and migration characteristics of bedforms under waves and currents. Part 1: Sandwave morphodynamics. *Coastal Engineering*, *53*(9), 767–780. https://doi.org/10.1016/j.coastaleng.2006.03.007

Clifton, H. E., & Dingler, J. R. (1984). Wave-formed structures and paleoenvironmental reconstruction. *Marine Geology*, *60*(1–4), 165–198. https://doi.org/10.1016/s0070-4571(08)70146-8

Colombini, M. (2004). Revisiting the linear theory of sand dune formation. *Journal of Fluid Mechanics*, *502*, 1–16. https://doi.org/10.1017/s0022112003007201

Colombini, M., & Stocchino, A. (2008). Finite-amplitude river dunes. *Journal of Fluid Mechanics*, *611*, 283–306. https://doi.org/10.1017/s0022112008002814

Damgaard, J., Soulsby, R., Peet, A., & Wright, S. (2003). Sand transport on steeply sloping plane and rippled beds. *Journal of Hydraulic Engineering*, *129*(9), 706–719. https://doi.org/10.1061/(ASCE)0733-9429(2003)129:9(706)

Damgaard, J., Whitehouse, R. J., & Soulsby, R. L. (1997). Bed-load sediment transport on steep longitudinal slopes. *Journal of Hydraulic Engineering*, *123*(12), 1130–1138. https://doi.org/10.1061/(ASCE)0733-9429(1997)123:12(1130)

Dean, R. G., & Dalrymple, R. A. (2004). *Coastal processes with engineering applications*. Cambridge University Press.

de Schipper, M. A., Hopkins, J., Wengrove, M. E., Saxoni, I., Kleinhans, M., Senechal, N., et al. (2019). Modex: Laboratory experiment exploring sediment spreading of a mound under waves and currents. In *Coastal sediments 2019: Proceedings of the 9th international conference on coastal sediments* (pp. 511–524). https://doi.org/10.1142/9789811204487_0046

De Vriend, H. n. (1987). 2dh mathematical modelling of morphological evolutions in shallow water. *Coastal Engineering*, *11*(1), 1–27. https://doi.org/10.1016/0378-3839(87)90037-8

Dey, S., & Ali, S. Z. (2020). Fluvial instabilities. *Physics of Fluids*, *32*(6), 061301. https://doi.org/10.1063/5.0010038

Dey, S., Mahato, R. K., & Ali, S. Z. (2022). Linear stability of sand waves sheared by a turbulent flow. *Environmental Fluid Mechanics*, *22*(2–3), 1–18. https://doi.org/10.1007/s10652-021-09813-6

Dey, S., Mahato, R. K., & Ali, S. Z. (2024). Linear and weakly nonlinear instabilities of sand waves caused by a turbulent flow. *Journal of Hydraulic Engineering*, *150*(3), 04024005. https://doi.org/10.1061/jhend8.hyeng-13760

Efron, B. (1982). *The jackknife, the bootstrap and other resampling plans*. SIAM.

Elias, E. P., & Hansen, J. E. (2013). Understanding processes controlling sediment transports at the mouth of a highly energetic inlet system (San Francisco Bay, ca). *Marine Geology*, *345*, 207–220. https://doi.org/10.1016/j.margeo.2012.07.003

Fredsoe, J., & Deigaard, R. (1992). *Mechanics of coastal sediment transport* (Vol. 3). World scientific publishing company.

Hardisty, J., & Whitehouse, R. (1988). Evidence for a new sand transport process from experiments on Saharan dunes. *Nature*, *332*(6164), 532–534. https://doi.org/10.1038/332532a0

Herrling, G., & Winter, C. (2014). Morphological and sedimentological response of a mixed-energy barrier island tidal inlet to storm and fair-weather conditions. *Earth Surface Dynamics*, *2*(1), 363–382. https://doi.org/10.5194/esurf-2-363-2014

Hsu, T.-J., & Hanes, D. M. (2004). Effects of wave shape on sheet flow sediment transport. *Journal of Geophysical Research*, *109*(C5), C05025. https://doi.org/10.1029/2003jc002075

Ikeda, S. (1982). Lateral bed load transport on side slopes. *Journal of the Hydraulics Division*, *108*(11), 1369–1373. https://doi.org/10.1061/jyceaj.0005937

Jones, K. R., & Traykovski, P. (2019). Interaction of superimposed megaripples and dunes in a tidally energetic environment. *Journal of Coastal Research*, *35*(5), 948–958. https://doi.org/10.2112/JCOASTRES-D-18-00084.1

Khelifa, A., & Ouellet, Y. (2000). Prediction of sand ripple geometry under waves and currents. *Journal of Waterway, Port, Coastal, and Ocean Engineering*, *126*(1), 14–22. https://doi.org/10.1061/(asce)0733-950x(2000)126:1(14)

Komar, P. D. (1977). Beach processes and sedimentation.

Lacy, J. R., Rubin, D. M., Ikeda, H., Mokudai, K., & Hanes, D. M. (2007). Bed forms created by simulated waves and currents in a large flume. *Journal of Geophysical Research*, *112*(C10), C10018. https://doi.org/10.1029/2006jc003942

Lee, S.-B. (2024). MODEX: Ripple geometry data [Dataset]. *Zenodo*. https://doi.org/10.5281/zenodo.10864976

Lee, S.-B., Wengrove, M. E., de Schipper, M. A., Hopkins, J., Kleinhans, M. G., & Ruessink, G. (2023). The contribution of sand ripple and slope driven sediment flux to morphologic change of an idealized mound under waves. *Journal of Geophysical Research: Earth Surface*, *128*(2), e2021JF006467. https://doi.org/10.1029/2021JF006467

Lee, S.-B., Wengrove, M. E., Hopkins, J., Saxini, I., & de Schipper, M. A. (2019). Wave driven sand ripple formation and evolution on a mound. In *Coastal sediments 2019: Proceedings of the 9th international conference* (pp. 615–626). https://doi.org/10.1142/9789811204487_0054

Lenstra, K. J., Pluis, S. R., Ridderinkhof, W., Ruessink, G., & van der Vegt, M. (2019). Cyclic channel-shoal dynamics at the ameland inlet: The impact on waves, tides, and sediment transport. *Ocean Dynamics*, *69*(4), 409–425. https://doi.org/10.1007/s10236-019-01249-3

Lesser, G. R., Roelvink, J. v., van Kester, J. T. M., & Stelling, G. (2004). Development and validation of a three-dimensional morphological model. *Coastal Engineering*, *51*(8–9), 883–915. https://doi.org/10.1016/j.coastaleng.2004.07.014

Li, M. Z., & Amos, C. L. (1998). Predicting ripple geometry and bed roughness under combined waves and currents in a Continental shelf environment. *Continental Shelf Research*, *18*(9), 941–970. https://doi.org/10.1016/s0278-4343(98)00034-x

Masselink, G., Austin, M., O'Hare, T., & Russell, P. (2007). Geometry and dynamics of wave ripples in the nearshore zone of a coarse sandy beach. *Journal of Geophysical Research*, *112*(C10). https://doi.org/10.1029/2006jc003839

Nielsen, P. (1981). Dynamics and geometry of wave-generated ripples. *Journal of Geophysical Research*, *86*(C7), 6467–6472. https://doi.org/10.1029/jc086ic07p06467

Nielsen, P. (1992). *Coastal bottom boundary layers and sediment transport* (Vol. 4). World Scientific.

O'Donoghue, T., Doucette, J., van der Werf, J. J., & Ribberink, J. S. (2006). The dimensions of sand ripples in full-scale oscillatory flows. *Coastal Engineering*, *53*(12), 997–1012. https://doi.org/10.1016/j.coastaleng.2006.06.008

Perillo, M. M., Best, J. L., & Garcia, M. H. (2014). A new phase diagram for combined-flow bedforms. *Journal of Sedimentary Research*, *84*(4), 301–313. https://doi.org/10.2110/jsr.2014.25

Ribberink, J. S., & Al-Salem, A. A. (1994). Sediment transport in oscillatory boundary layers in cases of rippled beds and sheet flow. *Journal of Geophysical Research*, *99*(C6), 12707–12727. https://doi.org/10.1029/94jc00380

Ruessink, G., Brinkkemper, J. A., & Kleinhans, M. G. (2015). Geometry of wave-formed orbital ripples in coarse sand. *Journal of Marine Science and Engineering*, *3*(4), 1568–1594. https://doi.org/10.3390/jmse3041568

Salimi-Tarazouj, A., Hsu, T.-J., Traykovski, P., & Chauchat, J. (2024). Investigating wave shape effect on sediment transport over migrating ripples using an Eulerian two-phase model. *Coastal Engineering*, *189*, 104470. https://doi.org/10.1016/j.coastaleng.2024.104470

Smith, E. R., Mohr, M. C., & Chader, S. A. (2017). Laboratory experiments on beach change due to nearshore mound placement. *Coastal Engineering*, *121*, 119–128. https://doi.org/10.1016/j.coastaleng.2016.12.010

Soulsby, R. (1997). *Dynamics of marine sands*. Thomas Telford Publications.

Soulsby, R. (2005). *Bedload transport under combined flows (tech. rep.)*. HR Wallingford.

Soulsby, R., Whitehouse, R., & Marten, K. (2012). Prediction of time-evolving sand ripples in shelf seas. *Continental Shelf Research*, *38*, 47–62. https://doi.org/10.1016/j.csr.2012.02.016

Soulsby, R., & Whitehouse, R. J. (1997). Threshold of sediment motion in coastal environments. *Pacific coasts and ports' 97: Proceedings of the 13th australasian coastal and ocean engineering conference and the 6th australasian port and harbour conference*, *1*, 145–150.

Stansby, P. K., Huang, J., Apsley, D. D., García-Hermosa, M. I., Borthwick, A. G. L., Taylor, P. H., & Soulsby, R. L. (2009). Fundamental study for morphodynamic modelling: Sand mounds in oscillatory flows. *Coastal Engineering*, *56*(4), 408–418. https://doi.org/10.1016/j.coastaleng.2008.09.011

Styles, R., & Glenn, S. M. (2000). Modeling stratified wave and current bottom boundary layers on the Continental shelf. *Journal of Geophysical Research*, *105*(C10), 24119–24139. https://doi.org/10.1029/2000jc900115

Tanaka, H., & Dang, V. T. (1996). Geometry of sand ripples due to combined wave-current flows. *Journal of Waterway, Port, Coastal, and Ocean Engineering*, *122*(6), 298–3000. https://doi.org/10.1061/(asce)0733-950x(1996)122:6(298)

Tonnon, P., Van Rijn, L., & Walstra, D. (2007). The morphodynamic modelling of tidal sand waves on the shoreface. *Coastal Engineering*, *54*(4), 279–296. https://doi.org/10.1016/j.coastaleng.2006.08.005

Traykovski, P. (2007). Observations of wave orbital scale ripples and a nonequilibrium time-dependent model. *Journal of Geophysical Research*, *112*(C6). https://doi.org/10.1029/2006jc003811

Van Rijn, L. C. (1993). Principles of sediment transport in Rivers, estuaries and coastal seas.

Wang, D., & Yuan, J. (2018). Bottom-slope-induced net sediment transport rate under oscillatory flows in the rippled-bed regime. *Journal of Geophysical Research: Oceans*, *123*(10), 7308–7331. https://doi.org/10.1029/2018jc013810

Wang, D., & Yuan, J. (2020). An experimental study of net sediment transport rate due to acceleration-skewed oscillatory flows over rippled seabeds. *Coastal Engineering*, *155*, 103583. https://doi.org/10.1016/j.coastaleng.2019.103583

Watanabe, A., & Sato, S. (2005). A sheet-flow transport rate formula for asymmetric, forward-leaning waves and currents. In *Coastal engineering 2004: (in 4 volumes)* (pp. 1703–1714). World Scientific.

Wengrove, M. E., de Schipper, M. A., Lippmann, T. C., & Foster, D. L. (2022). Surfzone bedform migration and sediment flux implications to large scale morphologic evolution. *Geomorphology*, *410*, 108246. https://doi.org/10.1016/j.geomorph.2022.108246

Wengrove, M. E., Foster, D. L., Lippmann, T. C., de Schipper, M. A., & Calantoni, J. (2018). Observations of time-dependent bedform transformation in combined wave-current flows. *Journal of Geophysical Research (Oceans)*, *123*(10), 7581–7598. https://doi.org/10.1029/2018jc014357

Wengrove, M. E., Foster, D. L., Lippmann, T. C., de Schipper, M. A., & Calantoni, J. (2019). Observations of bedform migration and bedload sediment transport in combined wave-current flows. *Journal of Geophysical Research (Oceans)*, *124*(7), 4572–4590. https://doi.org/10.1029/2018jc014555

Wiberg, P. L., & Harris, C. K. (1994). Ripple geometry in wave-dominated environments. *Journal of Geophysical Research*, *99*(C1), 775–789. https://doi.org/10.1029/93jc02726

Wright, L. D., & Short, A. D. (1984). Morphodynamic variability of surf zones and beaches: A synthesis. *Marine Geology*, *56*(1–4), 93–118. https://doi.org/10.1016/0025-3227(84)90008-2

Zijlema, M., & Stelling, G. S. (2005). Further experiences with computing non-hydrostatic free-surface flows involving water waves. *International Journal for Numerical Methods in Fluids*, *48*(2), 169–197. https://doi.org/10.1002/fld.821